

## Experimental Study on Acoustic and Aerodynamic Improvement of the Hemiptera-inspired Propeller Planform

Foad Moslem<sup>1</sup>, Mehran Masdari<sup>\*,1</sup>, Kirchu Fedir<sup>2</sup>, Behzad Moslem<sup>3</sup>

<sup>1</sup> Faculty of New Sciences and Technologies, University of Tehran, North Kargar Street, Tehran, 14395-1561, Iran

<sup>2</sup> Aviation Engines Department, National Aviation University, Liubomyra Huzara Ave, Kyiv, 03058, Ukraine

<sup>3</sup> Faculty of Industrial Engineering, Islamic Azad University Science and Research Branch, Tehran

### ARTICLE INFO

Received: 05 Sept. 2021;  
Received in revised form:  
14 Dec. 2021;  
Accepted: 23 Dec. 2021;  
Published online:  
06 Jan. 2022

#### Keywords:

Aeroacoustics  
Aerodynamic Performance  
Propeller  
Insect Bioinspiration  
Planform

### ABSTRACT

The multi-rotors have a short working duration and produce excessive noise, which is insufficient for complicated jobs and has a negative impact on human and animal health. Nonetheless, their market is growing in popularity. As a result, low-noise products are more competitive, and aerodynamic and acoustic enhancements are essential. The goal of this research is to create a small bioinspired propeller with the same power input as a conventional propeller that achieves the same or better aerodynamic performance while reducing noise. Accordingly, an experiment looked at the effects of different operating circumstances and geometric factors on the aerodynamic and aeroacoustic performance of a small propeller with a distinctive planform shape inspired by Hemiptera. This propeller was run at eleven rotational speeds ranging from 3000 to 8000 RPM with no freestream velocity to simulate hover circumstances. When compared to the baseline propeller, the Hemiptera propeller produce greater thrust for the same power source, reduce harmonic and broadband noise, and offer a better noise level. This noise reduction might be attributed to a decrease in Hemiptera propeller force fluctuation. Furthermore, its rotational speed is lower and its figure of merit is higher than the baseline propeller at hover flying with 3N thrust. Moreover, at this force, the Hemiptera propeller shows a 2.8W power reduction and a 5 dB decrease in acoustic signature. When it comes to hover efficiency, the Hemiptera propeller outperforms the baseline propeller across the board, regardless of thrust.

© Published at [www.ijtf.org](http://www.ijtf.org)

\*Corresponding e-mail: [m.masdari@ut.ac.ir](mailto:m.masdari@ut.ac.ir) (Mehran Masdari)

**Nomenclature**

$A$	Propeller disk area (m <sup>2</sup> )	$p_{ref}$	Reference pressure, $2 \times 10^{-5}$ Pa
$C_Q$	Coefficient of torque	$Q$	Torque (N.m)
$C_T$	Coefficient of thrust	$R$	Propeller radius (m)
$dB$	Decibel	$SPL_A$	A-weighted sound pressure level
$dB_A$	A-weighted decibel	$RPM$	Revolutions per minute
$FoM$	Figure of merit	$sUAS$	Small Unmanned Aerial Systems
$OASPL$	Overall A-weighted sound pressure level	$T$	Thrust (N)
$P_m$	Mechanical power	$UASs$	Unmanned Aerial Systems
$PL$	Power loading	$\rho$	Flow density (kg/m <sup>3</sup> )
$p_A$	Instantaneous sound pressure measured using the standard frequency weighting A	$\Omega$	Propeller rotational speed (rev/sec)

**1. Introduction**

The Unmanned Aerial Systems (UASs) market has grown in popularity for commercial, recreational, and scientific research purposes. Their appeal stems from their small size, low-cost electrical components, hovering and maneuvering capabilities, and user-friendly flying controllability. Various UAS systems have been presented as a new means of transportation and delivery over distances ranging from 1 to 300 km. Small Unmanned Aerial Systems (sUAS) are becoming a more common component of civilian activities, such as rescue operations, reaching hard-to-reach areas, and inspecting buildings. Multi-rotors are now the preferred sUAS platform, and their usage has increased. Multi-rotors currently have a low operational time of less than one hour, which is insufficient for complex tasks. Besides, the noise generated from the operating multi-rotors is another essential problem that can be limited to their use. Noise has adverse effects on humans' and animals' health, such as fatigue, mental illness, cognitive dysfunction, aggression, hormonal disorders, stress, stroke, heart attack, hypertension, diabetes, sleep disruption, and hearing impairment [1]. In other words, low-noise products are more competitive in the market, and aerodynamic and acoustic improvements are vital to increasing operational life and reducing noise.

The two primary noise sources of multi-rotors are the propellers and the motors. The propellers are the main source of lift generation and the predominant noise heard during flight phases under normal conditions, so in comparison, the noise of the motors can be ignored [2]. The propellers introduce complicated aerodynamic and aeroacoustic interactions that understanding their characteristics is critical for more efficient and quiet design. Figure 1 shows aerodynamic noise sources. Small propellers are operated at lower Reynolds number regimes ( $10^4 - 10^5$ ) and by decreasing the Reynolds number in this range, the lift decreases, whereas the drag increases. Propellers only have a few aerodynamic noise sources due to their size and Reynolds number regimes. A single propeller blade's noise mechanisms contribute to two main classes: broadband noise and harmonic noise. Harmonic noise includes thickness noise, loading noise, and blade-vortex interactions. Thickness noise is caused by the fluid being displaced around the blade as it turns and being directed towards the propeller plane. Loading noise is generated predominantly above and below the propeller plane due to the surface's steady and unsteady pressure loads. When the Mach number is less than one, the loading noise outweighs the harmonic noise. However, blade-vortex interaction (BVI) noise is heard when the

previously generated tip vortices and entrance blade collision. Broadband noise contains inflow turbulence and vortex noise. Inflow turbulence is present in broadband noise, and vortex noise is produced by the interaction of

the flow with various components of the blade, such as the leading edge, trailing edge, blade-tip, or turbulent flow in the wake.

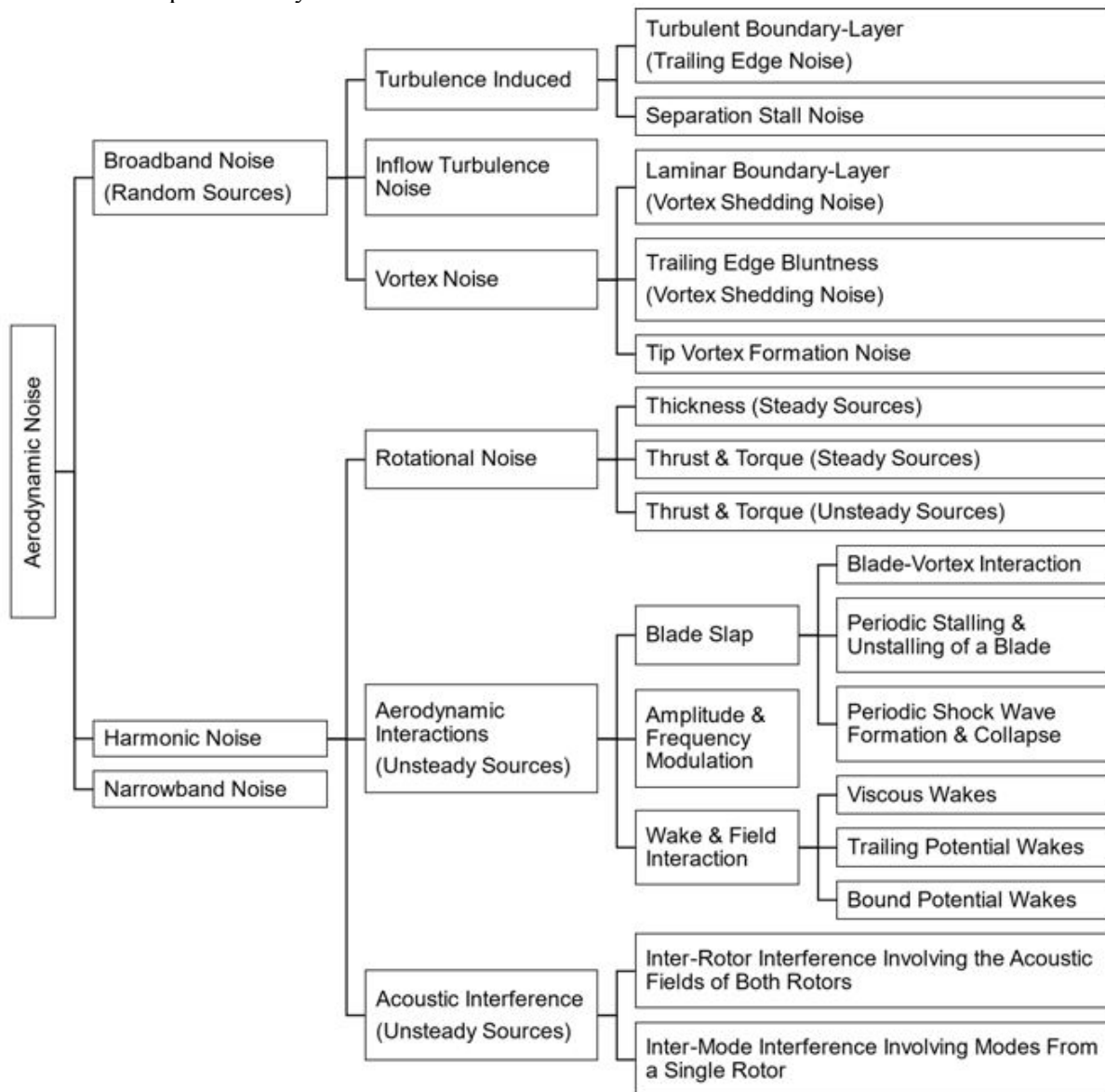


Fig. 1. Aerodynamic noise sources

There have been various noise reduction approaches to changing the design of the propeller blade, but these techniques must have no profound impact on aerodynamic performance and vehicle flight dynamics. Propeller noise studies, especially for larger vehicles like helicopters, focus on harmonic and impulsive noise sources. However, isolated small-scale propellers suffer from a

different type of noise [3]. Tonal noise in the low to mid-frequency region dominates isolated small-scale propellers, as it does full-scale propellers [4]. Broadband noise is substantial for small propellers at higher frequencies [5], [6]. In recent years, some experimental and numerical research has been done to understand and improve the aerodynamic performance and aeroacoustic

signatures of small propellers in different flight modes and conditions, such as hover flight, forward flight, and flight in harsh environments. Also, the effect of inflow disturbance and unsteady loading has been studied in some cases. Hovering quadrotors' noise signatures can be considerably decreased by replacing them with customized propellers. Zawodny and Boyd [7] studied hover acoustic measurements of isolated small propeller-airframe interactions. According to the analysis, under certain propeller tip clearance circumstances, the presence of the airframe surfaces might cause noise levels similar to or larger than the propeller blade surfaces. Thai and Grace [8] predicted thickness and loading noise directivity patterns for a small propeller in hover using CREATETM-AV Helios combined with the Ffowcs Williams-Hawkings solver. Whelchel, Alexander, and Intaratap [9] experimentally investigated the noise and thrust produced by four small propellers operating at takeoff conditions and propeller-airframe interaction and compared them with a DJI Matrice 600 Pro propeller. Carroll *et al.* [10] showed that small propellers could be produced rapidly for specific mission requirements. To produce geometries that meet user-specified performance requirements, a hybrid optimization technique is used with an aerodynamic performance algorithm. The model was validated experimentally using a propeller test stand capable of measuring both axial and non-axial performance. Brandt and Selig [11] tested 79 small propellers fitted in the 9- to 11-in diameter that operate in the low Reynolds number range of 50,000 to 100,000 to quantify propeller efficiency. Propeller efficiencies range from a high of 0.65 (for an efficient propeller) to a low of 0.28 (for an inefficient propeller). According to the findings, appropriate propeller selection for UAVs can have a significant impact on aircraft performance. Wisniewski *et al.* [12] analyzed thrust, sound pressure level (SPL), and RPM data from a DJI standard propeller and three custom-designed propellers at 1.4 lbf thrust. McKay and Kingan [13] observed that the minor variations in the small propeller's RPM produced unsteady loading and thickness noise, and after that, blade passing frequency

tones started showing up. Zawodny and Haskin [14] performed a subsequent detailed experimental investigation which showed how the relative importance of thickness and loading noise changed with observer position and how interference between the two noise sources could be important at specific locations. Casalino *et al.* [15] demonstrated the experimental and computational challenges of the benchmark configuration for small propeller aeroacoustics in the presence and absence of inflow, as well as the importance of fundamental research problems in transition and other low Reynolds number phenomena. Andria *et al.* [16] presented a way to improve small propeller performance. The modeling of the propeller's blades and hub, followed by simulation to estimate thrust, was the first step in this procedure. Finally, the thrust produced by different propellers was compared to better understand the changes that may be made. The aeroacoustic fingerprints of two small propellers were studied experimentally by Sinibaldi and Marino [17]. They observed that the improved propeller produces significantly less noise than the standard propeller at lower thrust settings.

Active and passive flow control techniques can be utilized to increase propeller performance and minimize noise. Active flow control methods are unviable for small propellers. On the other hand, passive flow control approaches manipulate the boundary layer without using any extra energy. They have been found to minimize noise production and are the focus of many studies. Leading and trailing edge patterns, porous materials, morphing, surface treatment, and dimples are the most common passive control approaches used to reduce noise generation. Because flying animals have evolved over millions of years to create efficient, high-performance wings, nature is an excellent source for passive flow control approaches for designing bioinspired wings. Yang, Wang, *et al.* [18] adopted an owl wing-inspired trailing-edge serrations for noise reduction of a small propeller and compared its aerodynamic and acoustic performance with a baseline propeller in the forward flight condition. Cambrey *et al.* [19] investigated the noise production process

from small propellers as well as the influence of trailing-edge serrations on noise reduction in their tests. Ning, Wlezien, and Hu [20] studied the noise attenuation capability of three distinct bio-inspired saw-tooth serrations applied to the baseline propeller to assess the serration's noise attenuation potential on a small propeller. To achieve maximal noise reduction while preserving aerodynamic power, Xiong, Nguyen, and Cramer [21] optimized an anti-phase alternating trailing-edge pattern for propeller noise suppression. Yang, Liu, Hu, *et al.* [22] presented a small wavy propeller and compared its aerodynamic and acoustic performance with a baseline propeller. Hintz *et al.* [23] presented experimental research findings to determine the influence of a bio-inspired blade planform on small-scale propeller thrust and energy consumption. Ning and Hu [24] examined a small propeller's aerodynamic and aeroacoustic properties with a novel planform shape inspired by the maple seed by comparing it to a typical baseline propeller in hover flight. They showed that the bioinspired propeller could provide equivalent thrust with constant power input while emitting less noise.

The goal of this research is to create a small bioinspired propeller that has the same power input as a conventional propeller and can achieve the same or better aerodynamic performance while reducing noise. Nature appears to have done an incredible job of designing insects' wings that are both practical and capable of sustained flight. Insects have different species, fly slower than birds, and operate at low Reynolds number flows. They take advantage of vortex patterns to provide the additional lift they require to fly [25]. Several studies have connected flow separation and vortex generation to insect flight's high lift aerodynamics [26]. The tip vortex adds significantly to the lift generated by a flat plate with an aspect ratio and motion amplitudes equal to those seen in nature, according to experimental studies [27]. Ning and Hu [24] showed that the majority of the thrust for a rotary-wing is known to be created between 50% and 90% of the propeller radius, and at Reynolds numbers ranging from 10,000 to 100,000, the lift to drag ratio dramatically

increases as the Reynolds number increases. As shown in Fig. 2, the Hemiptera (Cicada) wings' planform appears to be more compatible with the lift distribution, where the longest chord length is in the high lift area. As a result, if this planform configuration is used in the design, the propeller will operate at a better lift to drag ratio. Accordingly, an experimental test is mainly used to study a small propeller's aerodynamic and aeroacoustic performance with a unique planform shape inspired by Hemiptera (Cicada) wings. For the current investigation's comparison study, a typical tapered small-scale propeller was used as the baseline propeller.

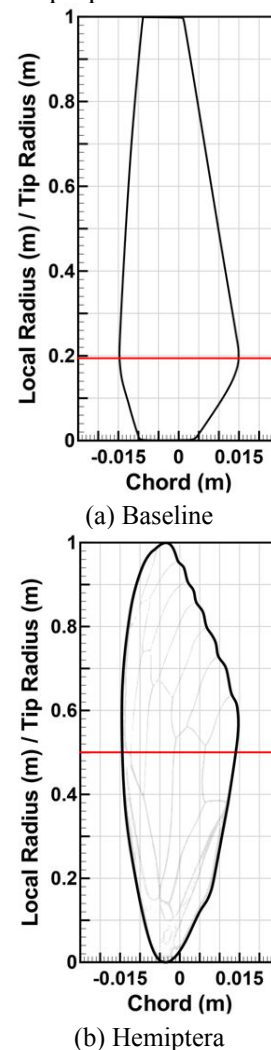


**Fig. 2** Baseline and Hemiptera wing planforms and their maximum chord location

The paper is organized as follows. The general phenomenon, the problem, cause of the problem, studies and solutions presented by

other authors, article objective, and solution have been shown in the introduction section. The two following sections deal with the methodologies used to analyze the aerodynamic and aeroacoustic properties of the propellers, as well as the experimental and numerical setup. Then, the third section reports and discusses the results. Eventually, Section four summarizes the investigation conclusions and describes future work and improvements.

## 2. Experimental Setup

The experiments were performed in the Experimental Aerodynamics and Aeroacoustics Research Laboratory's fully anechoic chamber at the University of Tehran. A schematic of the facility is sketched out in Fig. 3. The inner dimensions of the anechoic chamber from wedge tip to wedge tip are 3m long, 2.5m wide, and 2.56m tall with a low-frequency cut-off of 100 Hz. To reduce noise contamination, the propeller noise and loadings at the hover flight condition were measured using an external PC and DAQ.

Our experimental analysis compares the aeroacoustic features of two propellers with different planforms. We call the first one the baseline propeller and the bioinspired one the Hemiptera propeller. The shape of the baseline propeller is derived from a two-bladed 9450 model for the DJI Phantom II that has a 9.4" diameter and a pitch of 5.0", which is a small-scale commercial drone propeller used for video shooting and entertainment. The Hemiptera propeller's shape is inspired by a type of insect with about 50 to 80 thousand species, including cicadas. Their flying abilities are well developed for short distances and sporadically.

Based on Ning and Hu [24], the chord length from the largest chord on the planform to the propeller's tip decreased linearly. It was calculated by  $C_r = C_{tip}/r$ , where  $C_r$  is the chord length at the corresponding radius location, and  $r$  represents a non-dimensional

radial distance. The blade twisted 17.7 degrees at the largest chord on the planform to 4.7 degrees at the propeller's tip. Like Ning and Hu [24], due to a strength worry, we reshaped every single profile with a doubled thickness E63 airfoil based on the camber line and rescaled the diameter to 24cm fixed for both propellers, and our developed propellers achieved 0.12 solidity like other ordinary small propellers. The schematic and geometric details of both propellers are shown in Fig. 4. The propellers with a 0.1mm airfoil trailing edge thickness were manufactured using the Umbrel3d 3D printer with a 100 $\mu$ m resolution and a density of 20%, and were made by PLA material.

The experimental setup is shown in Fig. 3, which measures the thrust, torque, RPM, and sound pressure level. The testing equipment was positioned on a lab stand 6.25D above the surface such that the thrust was directed toward the chamber floor. The reflected noise from the floor was minimized by acoustic foam. When the propeller is in hover mode, the entire rig experiences nearly no vibration. For the measurement of the propeller thrust and torque, driven by an AIR 2213 electric brushless Tiger Motor with 920 KV, a three-component balance (a 30kg force capacity AmCells S-type and two 5kg force capacity YZC-133 loadcell) produced by the Experimental Aerodynamics and Aeroacoustics Research Group was located directly below the motor. An Agilent E3621A DC power supply provided power to the motor set at a constant 11.1 V for all tests. The propeller rotational speed was regulated using a T-Motor 20A AIR electronic speed controller, which received time pulse signals from an Arduino Uno and measured using a LUTRON DT-2268 tachometer. The T9545 propeller was tested to validate the aerodynamic facility's accuracy, and the results were compared to its datasheet, which showed the error was about 0.8%.

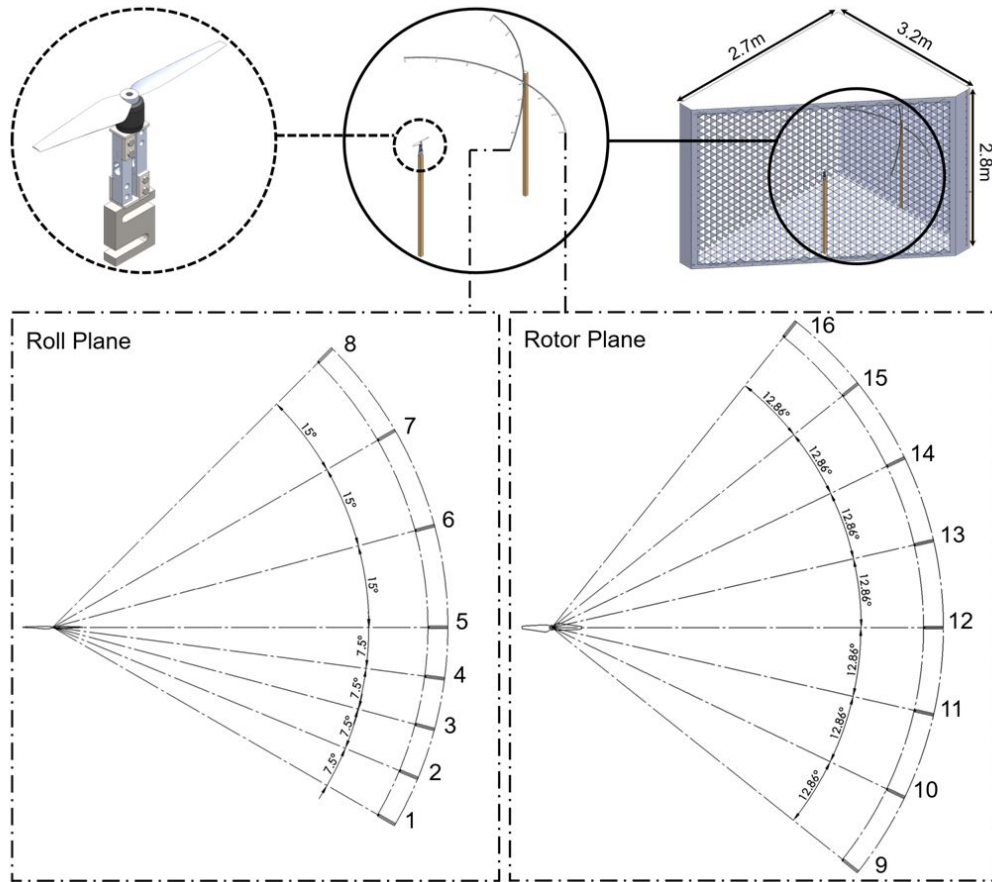


Fig. 3 Schematic of the facilities and microphone array

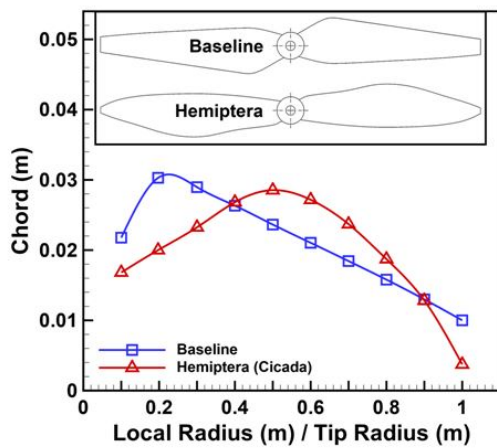


Fig. 4 Schematic and chord distribution of Hemiptera propeller compared to the baseline propeller

The microphone array is shown in Fig. 3. All acoustic measurements were made using fifteen 1/2 inch free-field Bruel & Kjaer microphones type 4190 microphones. The

microphones were configured on two crossed C-shaped arrays at a 6.25D radial distance from the center of the propeller and were positioned every 15° between 0° and 45° and every 7.5° between 0° and -30° on the roll-plane C-shape array configuration and every 13° on the propeller plane from the common microphone. The goal of this microphone array is to demonstrate noise reduction directivity and provide more accurate results than a single microphone. Wind-screens covered the microphones, and the frame was lined with absorbing material to reduce reflections. They were individually calibrated using a B&K Type 4231 sound calibrator. The calibrator showed ±0.2 dB calibration accuracy. The microphone's measurement uncertainty was ±1 dB up to 20 kHz. Noise measurements were performed on all microphones, but only results for microphone number five are reported for the sake of compactness. While acoustic pressure was recorded for 15 seconds at a sampling rate of 48 kHz, only the last 5

seconds of data was used to calculate the acoustic spectra. This time range was selected to consider only the steady-state noise. The thrust, torque, and rotation rates were recorded synchronously with the acoustic data. The balance data was collected for 5 seconds at a sampling rate of 2000 Hz. The thrust, torque, RPM, and microphone data were recorded using a LAN-XI DAQ data acquisition system and collected by an in-house developed data acquisition and control. For each Fourier transform, the recorded acoustic data was divided into time blocks of 1024 samples. Hanning windows were used, with a 50 percent overlap.

While investigating the impacts of propeller operation conditions and varied geometric parameters on aerodynamic loads and noise emissions, each propeller was operated at eleven rotational speeds ranging from 3000 rpm to 8000 rpm in 500 rpm increments. This rotation rate represents the typical RPM for small drones. Also, the freestream velocity was 0 m/s because the propeller was operated at a simulated hover condition. Representative values of local chord-based Reynolds and Mach numbers are displayed in Table 1.

Before testing in place, the load cells were calibrated by applying known weights to provide steady thrust and torque loads along the axis of each load cell, which covers the range of propeller loadings, and the calibration was verified before each set of tests. The thrust and torque measurement uncertainties were obtained at about 0.29% and 0.15% of the full range. The repeatability of 20 measurements on the baseline model at 3000, 5500, and 8000 RPM was used to calculate the uncertainty of the microphone data. The uncertainties for the

total noise's overall A-weighted sound pressure level (OASPL) were obtained at about 0.1 dB and 0.9 dB, respectively. The rotational speed uncertainty is 5 RPM, which can be ignored.

### 3. Flow Field Measurement

To better understand the complex unsteady flow fields, including velocity, vorticity, and noise reduction mechanisms of the bioinspired propeller concept, a 3D numerical simulation was performed based on a Lattice-Boltzmann method (LBM). The LBM defines fluid as a collection of separate, tiny, independent particles that can only exchange momentum when two particles collide. LBM's main idea is to statistically track these particles' advection and collisions using an integer number of distribution functions aligned with predetermined discrete directions. The Boltzmann transport equation is shown in Equation (1).

$$f_i(r + e_i, t + dt) = f_i(r, t) + \Omega_i(f_1, \dots, f_b), \quad i = 1, \dots, b. \quad (1)$$

where  $f_i$  is the distribution function in the direction  $i$ ,  $b$  is the number of velocity directions,  $r$  is the position on the lattice,  $e_i$  is the velocity in the  $i$  direction (m/s),  $t$  is the discrete-time (s), and  $\Omega_i$  is the collision operator.

The simulation focused on two rigid, fixed-pitch, two-bladed propellers operated at a rotation rate of 8000 RPM. The range of Reynolds numbers for baseline and Hemiptera propellers at different radial positions based on each section's chord length and linear velocity are shown in Table 1. The density and dynamic viscosity are selected as  $\rho = 1.225 \text{ Kg} \cdot \text{m}^{-3}$  and  $\mu = 1.789 \times 10^{-5} \text{ Pa} \cdot \text{s}$ . For the rotation rate of 8000 RPM, each simulation was run for 0.15 seconds (20 revolutions) with a two

**Table 1**  
local chord-based Reynolds and Mach numbers of propellers

Propeller	RPM	r/R	0.1	0.2	0.3	0.4	0.5	0.6	0.7	0.8	0.9	1
		-	Ma	3000	0.01	0.02	0.03	0.04	0.05	0.07	0.08	0.09

-		8000	0.03	0.06	0.09	0.12	0.15	0.18	0.21	0.23	0.26	0.29
Baseline	Re	3000	5431	15113	21676	26269	29482	31493	32200	31524	29162	24962
Hemiptera		3000	4196	9980	17399	26765	35594	40667	41384	37355	28790	9305
Baseline		8000	14482	40300	57803	70051	78618	83980	85868	84064	77764	66566
Hemiptera		8000	11189	26614	46397	71373	94917	108446	110356	99612	76774	24814

**Table 2**  
Grid independence analysis with baseline propeller

Grid	Elements ( $\times 10^6$ )	Thrust (N)	Relative Error in Thrust
Extra-Coarse	1	4.84	26.7
Coarse	2.2	4.21	10.1
Medium	3.4	4.01	4.9
Fine	4.3	3.91	2.3
Extra-Fine	6.1	3.90	2.1
Experimental	-	3.82	-

degrees azimuth time step, and the results were sampled for the last 0.075 seconds (10 revolutions). The simulation was performed in a rectangular domain that was 3.1m long, 3.1m wide, and 2.2m high. The fluid domain contains the propeller blades as solid boundary conditions and lateral walls, inlet, and outlet as far-field boundary conditions. At the boundaries of the propeller blades, an adiabatic wall with a non-slip boundary condition was utilized, whereas the lateral walls had a free slip boundary condition. The top and bottom boundary conditions were adjusted to have a velocity inlet of 0 m/s (hover condition) and a pressure outlet of zero-gauge pressure

(atmospheric conditions). The LES-WALE turbulence model was used. A grid independence study was performed using the baseline propeller to ensure that the mesh refinement did not affect the results, as shown in Table 2. The convergence criterion was based on the thrust, averaged for the last 0.075 s of the simulation. As a determination of the data's reliability, the thrust was compared with the measured experimental data. The Fine grid was chosen for the simulations that followed. As the data shows, there is good agreement between the experimental and simulation thrust of the propeller, and the error relative to the experimental thrust is only 2.3%. The far-field

scale is 0.0256 m in all cases. The resulting mesh size was about 4.3 million volume elements. All computations were performed on the Experimental Aerodynamics and Aeroacoustics Research Lab's computer at the Faculty of New Science and Technologies - the University of Tehran. It takes about two days to 20 revolutions on eight cores for each isolated propeller simulation.

#### 4. Results and Discussion

This section presents and discusses the contribution of a bioinspired planform to modifying small propeller aerodynamic efficiency and acoustic signature in two parts. In the first part, experimental aerodynamic performance is presented, and efficiency is studied, and in the last part, the experimental acoustic signature is investigated, and noise reduction is discussed.

##### 4.1 Experimental Aerodynamics Performance Results

The payload and endurance duration of multi-rotors are determined by aerodynamic performance. To characterize the designed propellers' performance, the coefficient of thrust ( $C_T$ ), coefficient of torque ( $C_Q$ ), mechanical power ( $P_m$ ), and figure of merit ( $FoM$ ) have been calculated, as shown in Equations (2), (3), (4), and (5) respectively, where  $\rho$  is flow density ( $kg/m^3$ ),  $A$  is the propeller disk area ( $m^2$ ),  $\Omega$  is propeller rotational speed ( $rev/sec$ ),  $R$  is propeller radius ( $m$ ),  $T$  is thrust ( $N$ ), and  $Q$  is torque ( $N \cdot m$ ). Also, the parameter of power loading ( $PL$ ) is defined as the available thrust for a given power in order to measure the efficiency of the rotors and is demonstrated by Equation (6).

$$C_T = \frac{T}{\rho A \Omega^2 R^2} \quad (2)$$

$$C_Q = \frac{Q}{\rho A \Omega^2 R^3} \quad (3)$$

$$P_m = Q \cdot \left( 2\pi \cdot \frac{RPM}{60} \right) \quad (4)$$

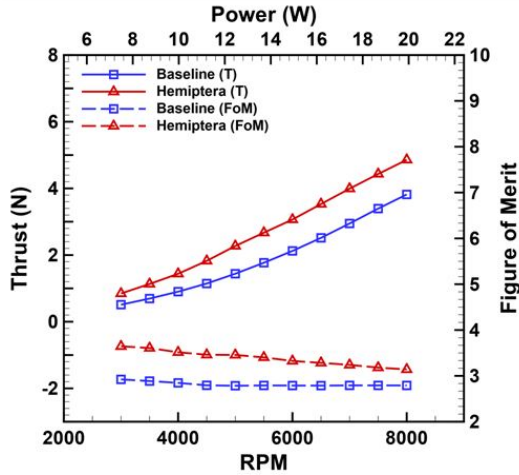
$$FoM = \frac{C_T^{3/2} / \sqrt{2}}{C_Q} \quad (5)$$

$$PL = T/P \quad (6)$$

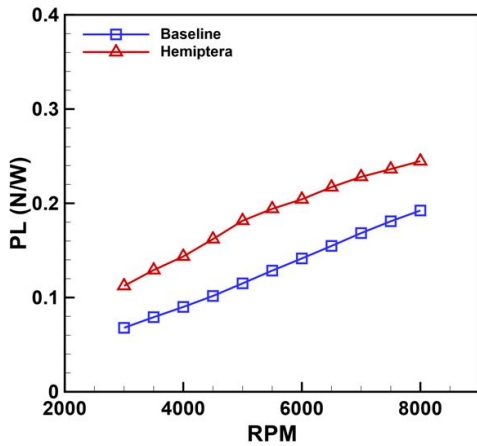
Figure 5 presents the comparative aerodynamic results. We utilize both dimensional and non-dimensional data in

propeller comparison, and there is no obligation to use just non-dimensional data. Furthermore, the sound pressure level is affected by the propeller's dimensional loading. The time-averaged thrust of the baseline and Hemiptera propellers increase from 0.51N and 0.85N to 3.82N and 4.86N when the rotational speed increase from 3000 RPM to 8000 RPM. The required time-averaged power of the baseline and Hemiptera propellers at hover flight with 3N thrust is 17.7W and 14.8W, and the power loading of these propellers is 0.17 N/W and 0.2 N/W. The results indicate that the Hemiptera propeller consumes 2.8W less power than the baseline propeller at hover flight. When the rotational speed increase from 3000 RPM to 8000 RPM, the power loading of the baseline and Hemiptera propellers increase from 0.07 N/W and 0.11 N/W to 0.19 N/W and 0.24 N/W, respectively. Therefore, the power loading of the Hemiptera-planform propeller in all RPM and thrust ranges is higher than the baseline. The results demonstrate that the Hemiptera propeller produces more thrust than the baseline propeller for the same power supply and generates less drag than the baseline propeller at hover flight with 3N thrust. With a maximum power decrease of 16.1% at hover flight, the Hemiptera propeller performs better than the baseline propeller. The rotational speed of the baseline and Hemiptera propellers at hover flight with 3N thrust is 7060 RPM and 5925 RPM, which shows Hemiptera is 18.9Hz slower than the baseline propeller at the same thrust. The drop in rotational speed shows that the thrust coefficient of the Hemiptera propeller is greater than that of the baseline propeller. The figure of merit of the baseline and Hemiptera propeller at hover flight with 3N thrust is 2.79 and 3.34. The figure of merit of the Hemiptera propeller at this thrust is about 19.5% higher than the baseline propeller, which leads to less torque or more thrust. At all thrust numbers evaluated, the Hemiptera propeller exhibits greater hover efficiency than the baseline propeller. This trend can be attributed to the largest chord length at 50% to 90% of the spanwise, which is known as the lift booster area, which means the Hemiptera

planform is beneficial in terms of aerodynamic efficiency.



(a) Thrust and Figure of Merit of baseline and Hemiptera propellers comparison in RPM and Power.



(b) Power Loading of baseline and Hemiptera propellers comparison in RPM

**Fig. 5** Aerodynamic performance results of Hemiptera compared to the baseline propeller.

A numerical simulation at 8000 RPM hover motion has been performed in addition to the experimental force measurements to demonstrate the planform's influence on the aerodynamic performance. Figure 6 shows the velocity and vorticity distributions of the baseline and Hemiptera propellers at 0, 45, 90, and 135-degree phase angles. As indicated by the 0-degree phase angle, the propeller is crossing the roll plane. The force produced by the spinning of the propeller pulls the flow into

the rotational plane and pushes it down to generate thrust. The shape of the vortices caused by the flow passing the trailing edge is significantly different between these two propellers. The induced velocity of the Hemiptera propeller is greater at the outer part as compared to the baseline propeller. The Hemiptera propeller has a higher velocity gradient than the baseline propeller from the outer part to the rotating axis. Because of the increased blade area, the friction drag of the Hemiptera propeller is higher than the baseline propeller, and the induced drag of the propellers is supposed to be the same as a result of the same tip vortex. As the phase angle rises, the tip vortex structure shifts inward and flows downstream. As confirmed in Fig. 6, the Hemiptera propeller pushes the wake vortices further from the trailing edge, thus decreasing the pressure drag. The flow that crosses the trailing edge causes weaker vortices along the span. These vortices travel quicker than tip vortices due to the velocity difference. The vortices formed at the blade's tip are more powerful than those formed at the blade's trailing edge. As a result, at around a 70 percent radius downstream, the next tip vortex interacts with the preceding one. This phenomenon is a common occurrence while the propeller is hovering. After the contact, a couple of tip vortices will form. Its power dwindles significantly and quickly disappears.

#### 4.2 Experimental Acoustics Signature Results

The aeroacoustic signature is characterized by an overall A-weighted sound pressure level (OASPL) at different frequencies and is calculated by Equations (7) and (8). Where  $SPL_A$  is A-weighted sound pressure level,  $p_A(t)$  is the instantaneous sound pressure measured using the standard frequency weighting A, and  $p_{ref}$  is the reference pressure and equal to  $2 \times 10^{-5} Pa$ .

$$OASPL = 10 \log \sum_{i=1}^n 10^{\frac{SPL_A}{10}} \quad (7)$$

$$SPL_A = 20 \log \left( \frac{p_A(t)}{p_{ref}} \right) \quad (8)$$

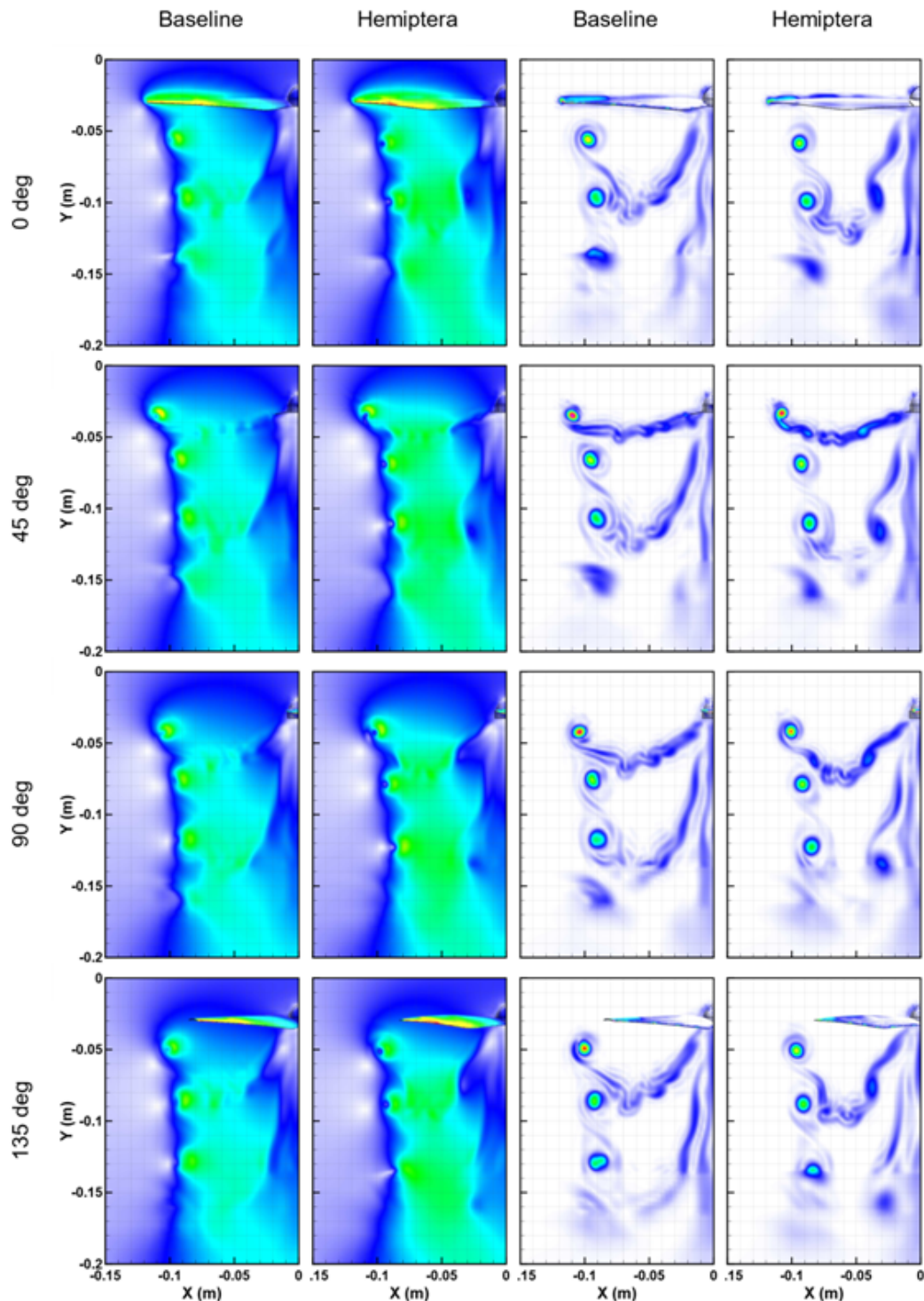


**Fig. 6** Velocity and vorticity distributions of baseline and Hemiptera propellers at hover flight with 3N thrust.

As shown in Fig. 7, mechanical noise (no propeller) has little influence at low frequencies (2500 Hz) but grows significantly above that frequency. Clearly, motor noise plays a key role in the system's stress noise at low frequencies. Also, Fig. 7 shows that the

Hemiptera propeller can decrease harmonic and broadband noise more effectively than the baseline propeller at hover flight with 3N thrust. Harmonic noise is associated with blade passing frequency and consists of loading and thickness noise. When the Mach number is less

than one, the loading noise takes precedence over the harmonic noise. However, it can decrease broadband noise more effectively than the baseline propeller at higher frequencies, due to the effect of the Hemiptera planform on the velocity gradient and pushing the wake vortices further from the trailing edge. This phenomenon reduces turbulent-boundary layer trailing edge noise and vortex shedding noise at the trailing edge and decreases inter-mode interference involving modes from the propeller apparent at higher frequencies. To better illustrate the differences in the graphs, the original graphs are shown in transparent and the ninth degree polynomial is shown in bold. This analysis helps to understand the noise characteristics of the bioinspired planform.

Figure 8 shows the OASPL directivity plot at hover flight with 3N thrust, and Fig. 9 indicates changing OASPL values of microphone number five versus RPM to evaluate the overall noise reduction. As we move up and down from microphone number five, the noise increases, which shows the loading, broadband, and blade-vortex interaction noise have overcome the thickness noise. The microphones on the roll plane show a distinct level of noise increasing and more noise emitting at the top of the roll plane. There is a slight variation in rotor plane microphone noises. As long as there is no interference from another rotor, the noise is virtually constant throughout the rotor plane. The OASPL of the baseline and Hemiptera propellers at microphone number five increase from 42.3 dB and 40.5 dB to 64.4 dB and 62.9 dB when the rotational speed increase from 3000 RPM to 8000 RPM. Also, the OASPL at hover flight with 3N thrust for these propellers is 60.4 dB and 55.4 dB, respectively. Figure 9 shows that in the range of 6000 RPM to 7000 RPM, the noise of the Hemiptera propeller is equal to the baseline propeller, but due to the difference in the generated thrust at the same RPM, the sound produced by the Hemiptera propeller is lower than the baseline propeller in all thrust ranges. Therefore, the results indicate that the Hemiptera propeller generates 5 dB less noise than the baseline propeller at

microphone number five and hover condition with 3N thrust.

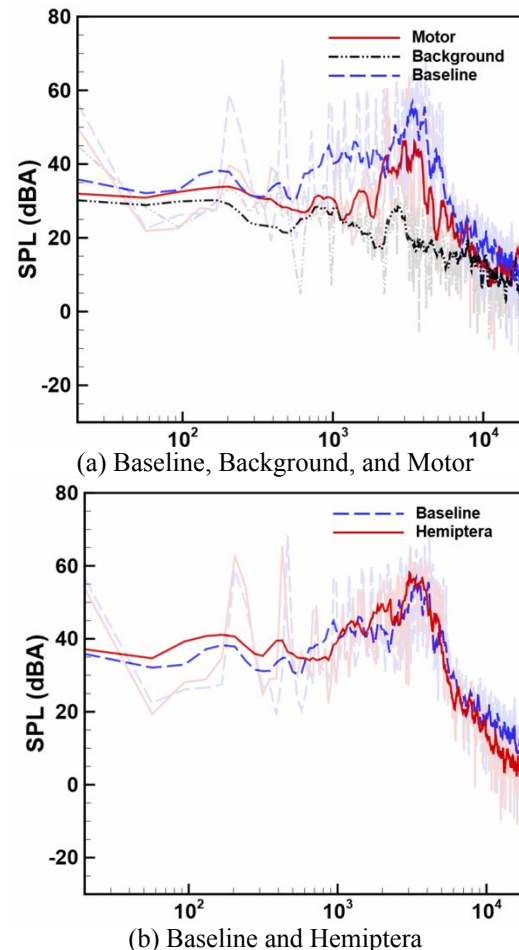
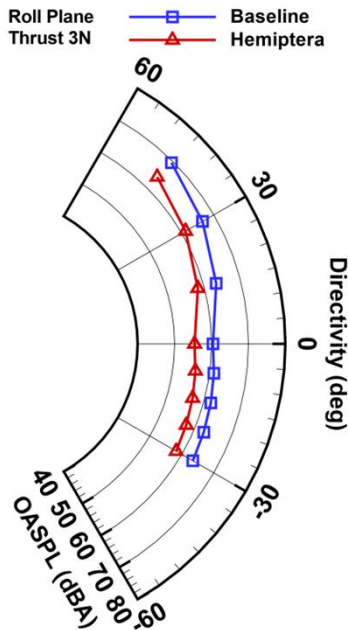
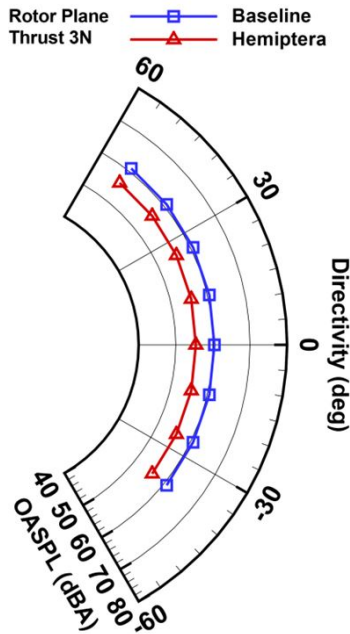


Fig. 7 Acoustic signature results compared to the baseline propeller at hover flight with 3N thrust (To better illustrate the differences in the graphs, the original graphs are shown in transparent and the ninth-degree polynomial is shown in bold.)

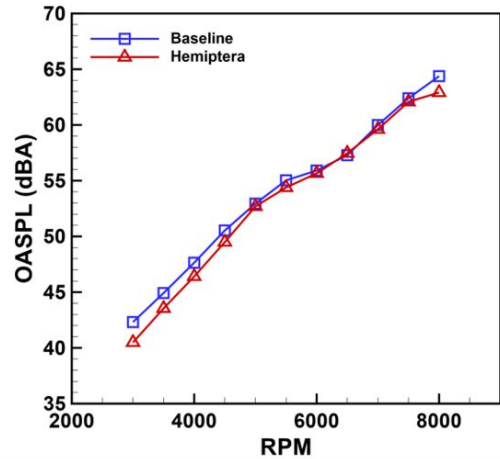


(a) Baseline and Hemiptera roll plane directivity comparison

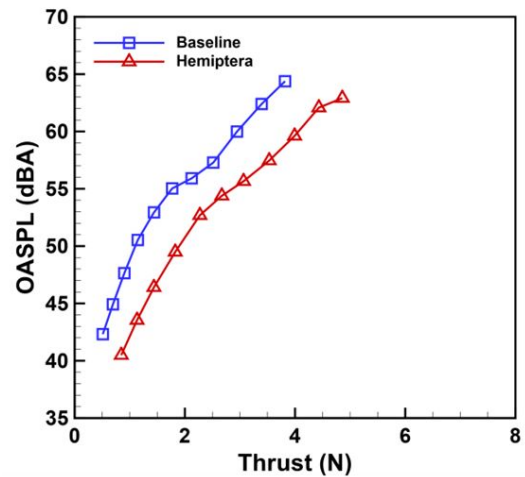


(b) Baseline and Hemiptera rotor plane directivity comparison

**Fig. 8** Hemiptera propeller noise directivity at hover flight with 3N thrust compared to the baseline propeller



(a) OASPL of baseline and Hemiptera propellers comparison in RPM



(b) OASPL of baseline and Hemiptera propellers comparison in thrust

**Fig. 9** Aeroacoustic performance results compared to the baseline propeller at microphone number five.

## 5. Conclusions

An experimental investigation investigated the impacts of operation conditions and varied geometric parameters on a small propeller's aerodynamic and aeroacoustic performance with a unique planform shape inspired by Hemiptera wings. Each propeller was operated at eleven rotational speeds ranging from 3000 to 8000 RPM with no freestream velocity for simulating hover conditions. Finally, using force and sound, a comparative experimental investigation into the aerodynamics and aeroacoustics characteristics of the baseline and bioinspired propellers was undertaken in an anechoic chamber. When compared to the baseline propeller, the Hemiptera propeller

produced greater thrust for the same power source, reduced harmonic and broadband noise, and offered a better noise level. This noise reduction might be attributed to a decrease in Hemiptera propeller force fluctuation. Furthermore, its rotational speed was lower and its figure of merit was higher than the baseline propeller at hover flying with 3N thrust. Moreover, at this force, the Hemiptera propeller shows a 2.8W power reduction and a 5 dB decrease in acoustic signature. When it came to hover efficiency, the Hemiptera propeller outperformed the baseline propeller across the board, regardless of thrust.

Future investigations will focus on some improvements. Xfoil should be utilized to guarantee that the best airfoil is chosen for each blade segment. Because noise generation is affected by blade quality vibrations, a high-resolution (25 $\mu$ m) 3D printed using a rigid material such as ABS plastic might offer accurate manufacturing precision. To increase structural stiffness, the airfoil section from  $r/R = 0.2$  should be smoothly integrated into the hub. To ensure reliable printing output, the trailing edge airfoil utilized along the propeller span (E63) should be thickened to 0.8 mm. The propeller should be connected from the top to a profiled aluminum testing rig for the least amount of interference. To decrease motor and test stand vibrations, a neoprene dampening material should be put directly beneath the load cell. The sampling rate may be increased to 80 kHz. The recording time may be increased by up to 20 seconds, and the data from the first 10 seconds could be utilized to compute acoustic spectra. It is necessary to investigate the effects of recirculation within the anechoic chamber. To get a frequency resolution of around 5 Hz, the number of FFT samples might be increased.

This study did not assess the influence of the existence of adjacent propellers and forward flight, which makes them a great target for future investigations. Furthermore, Smoke visualization, hotwire mapping, and PIV might be used to describe the downwash flow of a propeller, among other methods.

## Declaration of Conflicting Interests

The authors declare that there is no conflict of interest.

## References

- [1] Science for Environmental Policy, "FUTURE BRIEF: Noise Abatement Approaches," *EU Publ.*, no. 17, pp. 3–25, Apr. 2017, doi: 10.2779/016648.
- [2] R. S. McKay and M. J. Kingan, "Multi-rotor unmanned aerial system noise: Quantifying the motor's contribution," in *24th Acoustical Society of New Zealand Conference*, 2018, no. 1.
- [3] W. N. Alexander, J. Whelchel, N. Intaratep, and A. Trani, "Predicting community noise of sUAS," in *25th AIAA/CEAS Aeroacoustics Conference, 2019*, 2019, doi: 10.2514/6.2019-2686.
- [4] N. Intaratep, W. Nathan Alexander, W. J. Deveport, S. M. Grace, and A. Dropkin, "Experimental study of quadcopter acoustics and performance at static thrust conditions," in *22nd AIAA/CEAS Aeroacoustics Conference, 2016*, 2016, doi: 10.2514/6.2016-2873.
- [5] N. S. Zawodny, D. D. Boyd, and C. L. Burley, "Acoustic characterization and prediction of representative, small-scale rotary-wing unmanned aircraft system components," in *Annual Forum Proceedings - AHS International*, 2016, vol. 1–2016, pp. 34–48.
- [6] S. E. Wright, "The acoustic spectrum of axial flow machines," *J. Sound Vib.*, vol. 45, no. 2, pp. 165–223, 1976, doi: 10.1016/0022-460X(76)90596-4.
- [7] N. S. Zawodny and D. D. Boyd, "Investigation of rotor-airframe interaction noise associated with small-scale rotary-wing unmanned aircraft systems," *J. Am. Helicopter Soc.*, vol. 65, no. 1, 2020, doi: 10.4050/JAHS.65.012007.
- [8] A. D. Thai and S. M. Grace, "Prediction of small quadrotor blade induced noise," in *25th AIAA/CEAS Aeroacoustics Conference, 2019*, 2019, doi: 10.2514/6.2019-2684.
- [9] J. Whelchel, W. N. Alexander, and N. Intaratep, "Propeller noise in confined anechoic and open environments," in *AIAA Scitech 2020 Forum*, 2020, vol. 1 PartF, doi: 10.2514/6.2020-1252.
- [10] T. B. Carroll, I. R. George, G. Bramesfeld,

- and K. Raahemifar, "Design optimization of small rotors in quad-rotor configuration," in *54th AIAA Aerospace Sciences Meeting*, 2016, vol. 0, doi: 10.2514/6.2016-1788.
- [11] J. Brandt and M. Selig, "Propeller Performance Data at Low Reynolds Numbers," 2011, doi: 10.2514/6.2011-1255.
- [12] C. F. Wisniewski, A. R. Byerley, K. W. Van Treuren, and A. Hays, "Experimentally testing commercial and custom designed Quadcopter propeller static performance and noise generation," in *23rd AIAA/CEAS Aeroacoustics Conference, 2017*, 2017, doi: 10.2514/6.2017-3711.
- [13] R. S. McKay and M. J. Kingan, "Multirotor unmanned aerial system propeller noise caused by unsteady blade motion," in *25th AIAA/CEAS Aeroacoustics Conference, 2019*, 2019, doi: 10.2514/6.2019-2499.
- [14] N. S. Zawodny and H. H. Haskin, "Small propeller and rotor testing capabilities of the NASA langley low speed aeroacoustic wind tunnel," in *23rd AIAA/CEAS Aeroacoustics Conference, 2017*, 2017, doi: 10.2514/6.2017-3709.
- [15] D. Casalino, E. Grande, G. Romani, D. Ragni, and F. Avallone, "Towards the definition of a benchmark for low Reynolds number propeller aeroacoustics," in *Journal of Physics: Conference Series*, 2021, vol. 1909, no. 1, doi: 10.1088/1742-6596/1909/1/012013.
- [16] G. Andria *et al.*, "Design and performance evaluation of drone propellers," in *5th IEEE International Workshop on Metrology for AeroSpace, MetroAeroSpace 2018 - Proceedings*, 2018, pp. 407–412, doi: 10.1109/MetroAeroSpace.2018.8453604.
- [17] G. Sinibaldi and L. Marino, "Experimental analysis on the noise of propellers for small UAV," *Appl. Acoust.*, vol. 74, no. 1, pp. 79–88, 2013, doi: 10.1016/j.apacoust.2012.06.011.
- [18] Y. Yang, Y. Wang, Y. Liu, H. Hu, and Z. Li, "Noise reduction and aerodynamics of isolated multi-copter rotors with serrated trailing edges during forward flight," *J. Sound Vib.*, vol. 489, 2020, doi: 10.1016/j.jsv.2020.115688.
- [19] A. Cambray, E. Pang, S. A. Showkat Ali, D. Rezgui, and M. Azarpeyvand, "Investigation towards a better understanding of noise generation from UAV propellers," in *2018 AIAA/CEAS Aeroacoustics Conference*, 2018, doi: 10.2514/6.2018-3450.
- [20] Z. Ning, R. Wlezien, and H. Hu, "An experimental study on small UAV propellers with serrated trailing edges," in *47th AIAA Fluid Dynamics Conference, 2017*, 2017, doi: 10.2514/6.2017-3813.
- [21] J. Xiong, N. Nguyen, and N. B. Cramer, "Acoustic optimization for anti-phase asymmetric rotor," in *AIAA Scitech 2020 Forum*, 2020, vol. 1 PartF, doi: 10.2514/6.2020-1496.
- [22] Y. Yang *et al.*, "Experimental study on noise reduction of a wavy multi-copter rotor," *Appl. Acoust.*, vol. 165, 2020, doi: 10.1016/j.apacoust.2020.107311.
- [23] C. Hintz, P. Khanbolouki, A. M. Perez, M. Tehrani, and S. V. Poroseva, "Experimental study of the effects of bio-inspired blades and 3D printing on the performance of a small propeller," in *2018 Applied Aerodynamics Conference*, 2018, doi: 10.2514/6.2018-3645.
- [24] Z. Ning and H. Hu, "An experimental study on the aerodynamic and aeroacoustic performances of a bio-inspired UAV propeller," in *35th AIAA Applied Aerodynamics Conference, 2017*, 2017, doi: 10.2514/6.2017-3747.
- [25] Z. J. Wang, "Two dimensional mechanism for insect hovering," *Phys. Rev. Lett.*, vol. 85, no. 10, pp. 2216–2219, 2000, doi: 10.1103/PhysRevLett.85.2216.
- [26] J. Young, S. M. Walker, R. J. Bomphrey, G. K. Taylor, and A. L. R. Thomas, "Details of insect wing design and deformation enhance aerodynamic function and flight efficiency," *Science (80-. )*, vol. 325, no. 5947, pp. 1549–1552, 2009, doi: 10.1126/science.1175928.
- [27] M. J. Ringuette, M. Milano, and M. Gharib, "Role of the tip vortex in the force generation of low-aspect-ratio normal flat plates," *J. Fluid Mech.*, vol. 581, pp. 453–468, 2007, doi: 10.1017/S0022112007005976.